


Frequency-Selected Bifunctional Coding Acoustic Metasurfaces

Ya Zhang¹,^{*} Hua Cheng^{1,*}, Jianguo Tian^{1,†} and Shuqi Chen^{1,2,3,‡}

¹The Key Laboratory of Weak Light Nonlinear Photonics, Ministry of Education, School of Physics and TEDA Institute of Applied Physics, Nankai University, Tianjin 300071, China

²The Collaborative Innovation Center of Extreme Optics, Shanxi University, Taiyuan, Shanxi 030006, China

³Collaborative Innovation Center of Light Manipulations and Applications, Shandong Normal University, Jinan 250358, China

 (Received 22 June 2020; revised 1 November 2020; accepted 18 November 2020; published 18 December 2020)

Coding metasurfaces are a kind of metasurface that can combine artificial structures with digital codes “0” and “1.” By digitally programming the arrangements of structural units, they can manipulate the transmitted or reflected waves into arbitrary patterns. Recently, coding metasurfaces have been demonstrated to realize fascinating functions in acoustics, including far-field modulation, focusing, and vortex beam generation. However, the previous acoustic coding metasurfaces work at a single frequency and have only one function under a specific arrangement, limiting the efficiency and capacity of manipulation to a low quality. To overcome these shortcomings, here we propose frequency-selected bifunctional coding acoustic metasurfaces. Dual-layer Helmholtz-like resonators are utilized to produce a 0 and π phase difference, corresponding to the “0” and “1” codes, respectively. Owing to the design of the dual-layer resonators, the two working frequencies are integrated on a single unit with a subwavelength thickness, which eliminates the long-wavelength limitations. Frequency-selected anomalous reflection, diffusion, and Airy-beam generation are further demonstrated to prove its availability. The results are shown through theoretical predictions, simulations, and experiments, which show good correspondence. The proposed frequency-selected bifunctional coding acoustic metasurfaces can be used in acoustic information preservation and provide an alternative way to achieve multispectral acoustic devices.

DOI: [10.1103/PhysRevApplied.14.064057](https://doi.org/10.1103/PhysRevApplied.14.064057)

I. INTRODUCTION

Metasurfaces, as the two-dimensional (2D) version of metamaterials with subwavelength thicknesses, have been a hot topic in recent years due to their outstanding capabilities in the manipulation of wave propagation. Basically, metasurfaces are composed of meta-atoms and modulate the wave fronts by controlling the wave response of each meta-atom; thus arbitrary wave fronts can be achieved and numerous functions have been found, such as anomalous reflection and refraction [1–11], perfect absorption [12–14], and asymmetric propagation [15–17]. Recently, metasurfaces that can achieve multifunctions have received more and more attention, since there is a strong expectation of one single metasurface that can deal with concurrent tasks [18]. Frequency-selected multifunctional metasurfaces are a kind of multifunctional metasurface that has different functions at different frequencies. In acoustics, two methods are proposed to design frequency-selected

multifunctional metasurfaces. One is to use the supercells, in which each cell corresponds to one frequency and a specific function [19,20]. Obviously, this design acquires multioptimization of the structures. Another is to use the nonresonant mechanism so that harmonic frequencies can work at each meta-atom [21]. However, such a design is limited at low frequency as the wavelength becomes very large.

Nowadays, a kind of digital metamaterial, termed a coding metamaterial, has been proposed for the purpose of simplifying the structure with limited units and controlling the waves in a more flexible way [22]. The simplest coding metamaterial contains only two types of coding units, “0” and “1,” which are related to the “0” and “ π ” phase responses and correspond to the *on* and *off* states, respectively [22]. Subsequent to the work of Cui *et al.*, there has been a boom in the field of coding metamaterials and the idea has been extended to multibit, multiband, and time-modulation coding metamaterials and metasurfaces; thus many complicated functions have been achieved, including diffusion, vortex-beam generation, and holographic imaging [22–28]. Owing to the simplicity and flexibility of coding metamaterials, the concept has subsequently

*Corresponding author. hcheng@nankai.edu.cn

†Corresponding author. jjtian@nankai.edu.cn

‡Corresponding author. schen@nankai.edu.cn

been introduced to acoustics [29–31], nonlinear optical metasurfaces [32], and topological structures [33]. By defining “0” and “1” codes with different phase responses (0 and π) or different topological states (trivial and nontrivial) and arranging these units in arbitrary patterns, coding metamaterials can manipulate the wave propagation in an efficient and simple way. However, the previous acoustic coding metasurfaces work at a single frequency and have only one function when the coding pattern is specified. The realization of frequency-selected multifunctional acoustic coding metasurfaces still remains a challenge.

Here, we propose frequency-selected bifunctional coding acoustic metasurfaces based on a two-layer Helmholtz-resonator-like structure. Four types of coding units are selected as the “0” and “1” codes working independently at two specific frequencies. By arranging these coding units in different patterns, we demonstrate the functions of frequency-selected anomalous reflection, acoustic diffusion, and acoustic Airy-beam generation through theoretical predictions, numerical simulations, and experiments, which are in satisfactory agreement. Compared with conventional frequency-selected acoustic metasurfaces, the proposed frequency-selected bifunctional coding acoustic metasurfaces distribute the frequency-selected functions into each meta-atom without a nonresonance mechanism. The proposed design has a high working efficiency and removes the long-wavelength limitation, which opens up an alternative way to design frequency-selected multifunctional acoustic devices.

II. DESIGN

The conceptual schematic of the frequency-selected bifunctional acoustic metasurface is illustrated in Fig. 1(a). For frequency f_1 , the coding sequence is “010101.../010101...” in the x direction; for frequency f_2 , the coding sequence is “010101.../010101...” in the y direction. Thus, normally incident acoustic waves containing frequencies f_1 and f_2 will be reflected in two directions on the x - z plane and the y - z plane at the two frequencies, respectively. The coding unit that makes up the metasurfaces is shown in Fig. 1(b) and has a two-layer Helmholtz-resonator-like design. The two layers are connected in series, with a side length $p = 3$ cm and a whole thickness $H = 0.8$ cm. The cavities on the two layers have the same side length $D = 2.4$ cm, but different heights, $h_1 = 0.3$ cm and $h_2 = 0.2$ cm, for the upper and lower ones, respectively. The two necks on both layers have the same thickness $t = 0.1$ cm and changeable side lengths d_1 and d_2 for the upper and lower ones. To optimize the parameters of the coding unit, we make simulations to obtain its phase response, utilizing the commercial COMSOL Multiphysics software, which is based on the finite-element method [34]. The material of the coding unit is set as acoustically rigid and the coding unit is immersed in air

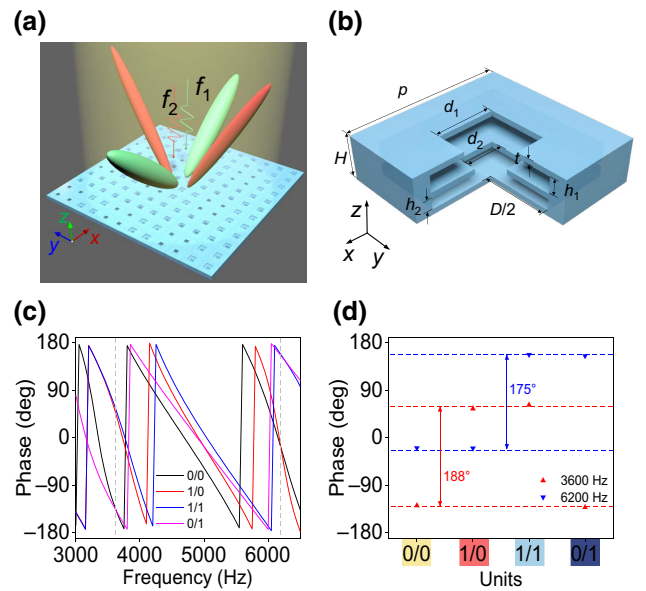


FIG. 1. The schematic of (a) the frequency-selected bifunctional metasurface and (b) the coding unit. (c) Simulated reflected phases versus the frequencies of incident acoustic waves, where the lines with different colors represent units with different structure parameters. (d) The extracted phase responses of four units at $f_1 = 3600$ Hz and $f_2 = 6200$ Hz.

is described by the density $\rho = 1.21$ kg/m³ and the sound speed $c = 343$ m/s. As the coding metasurface works independently at two frequencies, there are at least four optimized coding units for our frequency-selected bifunctional metasurfaces, the parameters d_1 and d_2 of which are shown in Table I. The codes before and after the symbol “/” represent the codes at frequency f_1 and f_2 , respectively. By appropriately adjusting the dimensions or geometries of the designed Helmholtz resonators, the two working frequencies can also be further adjusted to improve the functionality of our design, i.e., the two working frequencies can be monotonously adjusted by simultaneously changing the periodicity p and the side length D while keeping $p - D$ constant, which can cover a large range of working frequencies. Figure 1(c) illustrates the phase responses of the four units at different frequencies, from which we find that two of the four coding units work as “0” and the other two work as “1” at the frequency of $f_1 = 3600$ Hz ($f_2 = 6200$ Hz). For a clearer display, we extract the required phase responses of the four coding units at the two working frequencies, marked as red triangles for f_1 and blue inverted triangles for f_2 in Fig. 1(d). The phase difference between the “0” and the “1” states cannot reach the exact 180° , as the existing coupling between the top and bottom connected resonators results in imperfect phase reversion during the resonances. But the error is in acceptable and hardly influences the performance of the coding metasurfaces.

TABLE I. The optimized parameters of the four coding units.

Units	d_1 (cm)	d_2 (cm)
0/0	1.2	0.5
1/0	1.1	0.7
1/1	1.0	0.9
0/1	0.7	1.4

III. EXPERIMENTS AND DISCUSSION

We now program the coding metasurfaces with the four coding units. To prove the frequency-selected bifunctional properties of the metasurfaces, we attempt to study three functions commonly realized in traditional metasurfaces, involving anomalous reflection, diffusion, and the Airy beam. Thus, three 2D coding metasurfaces with sequences S_1 (with subsequences “0101.../0101...” in the x direction for f_1 and “0101.../0101...” in the y direction for f_2), S_2 (with subsequences “0101.../0101...” in the x direction for f_1 and “0101.../1010...” in the x direction for f_2), and S_3 (with subsequences “001011” on both the x and y axes for f_1 and f_2) and a single one-dimensional (1D) coding metasurface with sequence S_4 (with subsequences “011100011100001111000001111111” and “111110001100011001101100100100” for f_1 and f_2 , respectively) are considered, in which S_1 and S_2 are used for anomalous reflection, S_3 is used for diffusion, and S_4 is used for generating the Airy beam. Accounting for the limitation of the working frequencies, the “ 2×2 ” subarrays of the coding units are utilized as the fundamental lattices to build the 2D coding metasurfaces. Samples are exhibited in Fig. 2(a), all of which are fabricated with photosensitive resin, utilizing 3D-printing technology. For the 2D metasurfaces S_1 , S_2 , and S_3 , the measurements are carried out in free space, as shown in Fig. 2(b), from which we can directly obtain the far-field and near-field distributions by scanning the microphone on the dot-line half-circle (with a radius of 1 m for S_1 and S_2 and 5 m for S_3) and the gray half-transport area, respectively. A circular planar speaker (JBL CSS8006BM, diameter 200 mm) is employed as the sound source to make a plane wave illuminating on the metasurfaces. For the measurement of the 1D metasurfaces S_4 , an acoustic waveguide is needed, as illustrated in Fig. 2(c), which is built using two pieces of acrylic plate and absorbing foams on the boundaries to decrease multireflections. An array of speakers with a spacing distance of 3 cm is used as the plane-wave sound source, placed opposite to the sample array. All measurements are accomplished by a multianalyzer system (B&K Type 3560B) containing a pulse generator (B&K Type 3160) and two microphones (B&K 4961, 1/4-in. diameter). Step distances of 2 cm and 1 cm are used in field scanning for f_1 and f_2 , respectively.

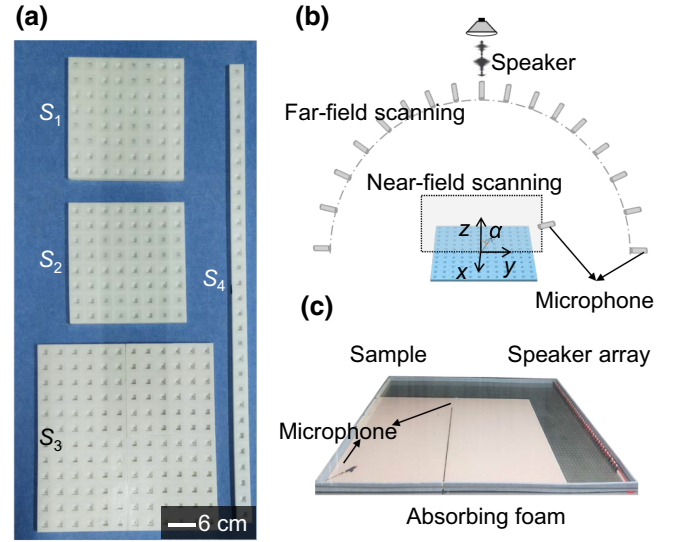


FIG. 2. (a) A photograph of the three-dimensionally (3D) printed samples S_1 , S_2 , S_3 , and S_4 . S_1 is subcoded with the subsequences “0101.../0101...” in the x direction for f_1 and “0101.../0101...” in the y direction for f_2 ; S_2 is subcoded with the subsequences “0101.../0101...” in the x direction for f_1 and “0101.../1010...” in the x direction for f_2 ; S_3 is subcoded with the subsequences “001011” on both the x and y axes for f_1 and f_2 ; and S_4 is subcoded with the subsequences “011100011100001111000001111111” and “111110001100011001101100100100” for f_1 and f_2 , respectively. (b),(c) Measurement setups for (b) sample S_1 , S_2 and S_3 (c) sample S_4 .

A. Frequency-selected wave splittings

Taking 2D metasurfaces with sequences S_1 and S_2 as examples, we first discuss the function of anomalous reflection. When an acoustic wave normally illuminates a 2D coding metasurface encoded with $N \times N$ equal-sized lattices, the reflected far-field pattern can be expressed as [22–29]

$$F(\theta, \varphi) = F_e(\theta, \varphi) \sum_{m=1}^N \sum_{n=1}^N \exp \left\{ -i \left\{ \varphi(m, n) + kP \sin \theta \left[\left(m - \frac{1}{2} \right) \cos \varphi + \left(n - \frac{1}{2} \right) \sin \varphi \right] \right\} \right\}, \quad (1)$$

where $\varphi(m, n)$ is either “0” or “ π ” for the mn lattice; θ and φ are the elevation and azimuth angle of an arbitrary direction, respectively; P is the lattice constant, equal to $2p$; k is the wave vector of the acoustic wave; and $F_e(\theta, \varphi)$ is the function of a lattice pattern. The coding sequence S_1 contains two different subcoding sequences: “0101.../0101...” along the x direction for f_1 and “0101.../0101...” along the y direction for f_2 . The reflected far-field patterns can be numerically calculated

using Eq. (1) as

$$|F_{11}(\theta, \varphi)| = 2C_1 \left| \cos \frac{\psi_1 + \psi_2}{2} \sin \frac{\psi_1 - \psi_2}{2} \right|, \quad (2)$$

$$|F_{12}(\theta, \varphi)| = 2C_1 \left| \sin \frac{\psi_1 + \psi_2}{2} \cos \frac{\psi_1 - \psi_2}{2} \right|, \quad (3)$$

where $\psi_1 = kP \sin \theta (\sin \varphi + \cos \varphi)/2$, $\psi_2 = kP \sin \theta (\sin \varphi - \cos \varphi)/2$, C_1 is a constant and the subscripts “11” and “12” represent the reflected far-field patterns of S_1 for f_1 and f_2 , respectively. The maxima are achieved when $|\cos[(\psi_1 + \psi_2)/2] \sin[(\psi_1 - \psi_2)/2]| = 1$ for f_1 and $|\sin[(\psi_1 + \psi_2)/2] \cos[(\psi_1 - \psi_2)/2]| = 1$ for f_2 . Then $\theta_{11} = \arcsin(\lambda_1/2P) = 52.6^\circ$, $\varphi_{11} = 0^\circ$ and 180° , $\theta_{12} = \arcsin(\lambda_2/2P) = 27.5^\circ$, $\varphi_{12} = 90^\circ$ and 270° can be obtained for f_1 and f_2 , respectively. Thus, a normally incident wave with a frequency of f_1 (f_2) is reflected in two symmetric directions with respect to the z axis on the x - z (y - z) plane, as shown in Fig. 3(a) [Fig. 3(b)]. To carefully examine the reflected far-field patterns, the 1D expansion of the normalized far-field patterns versus the reflected angle are, respectively, given in Figs. 3(e) and 3(f) for f_1 and f_2 , with the line representing the simulated results and the dots representing the measured results, in which two peaks for each frequency can be clearly observed and the energy is more concentrated on the maximum for a higher frequency.

Figures 3(i) and 3(m) [Figs. 3(j) and 3(n)] show the simulated and measured pressure distributions for f_1 (f_2), respectively, where the reflected quasiplane waves propagate in two symmetric directions with respect to the z axis on the x - z (y - z) plane for f_1 (f_2), with a standing-wave-like area formed in the center. As the acoustic wave with a smaller wavelength is more sensitive to the experimental environment, the measured pressure distribution for f_2 has a lower quality than f_1 . Similarly, for sequence S_2 , which is encoded with subsequences “0101.../0101...” for f_1 and “0101.../1010...” for f_2 , the reflected far-field patterns can also be derived as $|F_{21}(\theta, \varphi)| = 2C_1 |\cos[(\psi_1 + \psi_2)/2] \sin[(\psi_1 - \psi_2)/2]|$ and $|F_{22}(\theta, \varphi)| = 2C_1 |\sin[(\psi_1 + \psi_2)/2] \cos[(\psi_1 - \psi_2)/2]|$. The extremal points are achieved at $\theta_{21} = \arcsin(\lambda_1/2P) = 52.6^\circ$, $\varphi_{21} = 0^\circ$ and 180° for f_1 , $\theta_{22} = \arcsin(\lambda_2/\sqrt{2}P) = 40.7^\circ$, $\varphi_{21} = 45^\circ, 135^\circ, 225^\circ$ and 315° for f_2 . Then, the incident wave splits into two branches for f_1 and four branches for f_2 , as shown in Figs. 3(c) and 3(d).

Figures 3(g) and 3(h) give the 1D far-field distributions on the x - z and $y = -x$ planes for f_1 and f_2 , respectively, where two peaks can be found for each frequency and the reflected angle for f_2 is bigger than that of S_1 , consistent with the theoretical prediction. Corresponding pressure distributions are shown in Figs. 3(k) and 3(o)

for f_1 and Figs. 3(l) and 3(p) for f_2 , with the simulated results in Figs. 3(k) and 3(l) and the measured results in Figs. 3(o) and 3(p). To evaluate the performance of the wave-branching functions, we calculate the signal-to-noise ratios (SNRs) for S_1 and S_2 . The SNR is defined as $\text{SNR} = E_s/(E_0 - E_s)$, where the E_s and E_0 are the effective and whole signal intensities, respectively. The E_s is defined as the signal exceeding $1/e$ of the peak intensity around the designed angle. The SNRs are 3.08 (f_1), and 5.25 (f_2) for S_1 , 3.32 (f_1), and 4.43 (f_2) for S_2 , respectively. The SNRs at f_1 are lower than that at f_2 for the two metasurfaces, indicating that the devices can work more efficiently at a higher frequency. The SNR also can be further improved by increasing the number of coding lattices.

B. Frequency-selected diffusions

When the incident acoustic wave is reflected in a sufficient number of directions and the energy is evenly distributed in each direction, we obtain another application—diffusion. Research on acoustic diffusion originates from echo control of the music in a large auditorium, where the energy of the echo should be preserved rather than absorbed to avoid the loss of sound. One of the most significant occurrences in diffuser design was the invention of the phase-grating diffuser by Schroeder [35], leading to the flourishing development of Schroeder diffusers in the years that followed. Nevertheless, the large thicknesses limit their applications when the frequency is low. To overcome this limitation, Zhu *et al.* proposed an ultrathin design of Schroeder diffuser in 2017 [36], based on Helmholtz-like resonators. The ultrathin Schroeder diffuser has a thickness of only 1/20th of the working wavelength, which is 1/10th of that of the traditional Schroeder diffuser. However, the working frequency of one unit has been limited to a single frequency due to the resonating nature. Thus, our proposed frequency-selected coding units can be utilized well to realize a frequency-selected acoustic diffuser. The diffusion can be reached by minimizing the directivity of the reflected acoustic waves, which can be described by the reduction of the radar cross sections (RCS) [22]. By optimizing the coding sequence with “0” and “1” lattices, the best RCS reduction can be achieved and the optimized sequence for diffusion is obtained as “001011” along both the x and y axes for a 6×6 array. According to the derivation of Eq. (1), the reflected directions will increase and the energy will be discretely distributed in these directions. The simulated 3D reflected far-field patterns of S_3 are shown in Fig. 4(a) for f_1 and in Fig. 4(c) for f_2 . Figures 4(b) and 4(d) are obtained by illuminating the plane wave on a flat plate, which works as the reference. To compare the reflected energy in different reflection angles of the metasurface with that of the plate, we extract the 1D normalized far-field patterns on the x - z plane versus the reflected angle for f_1 and f_2 , shown in Figs. 4(e) and

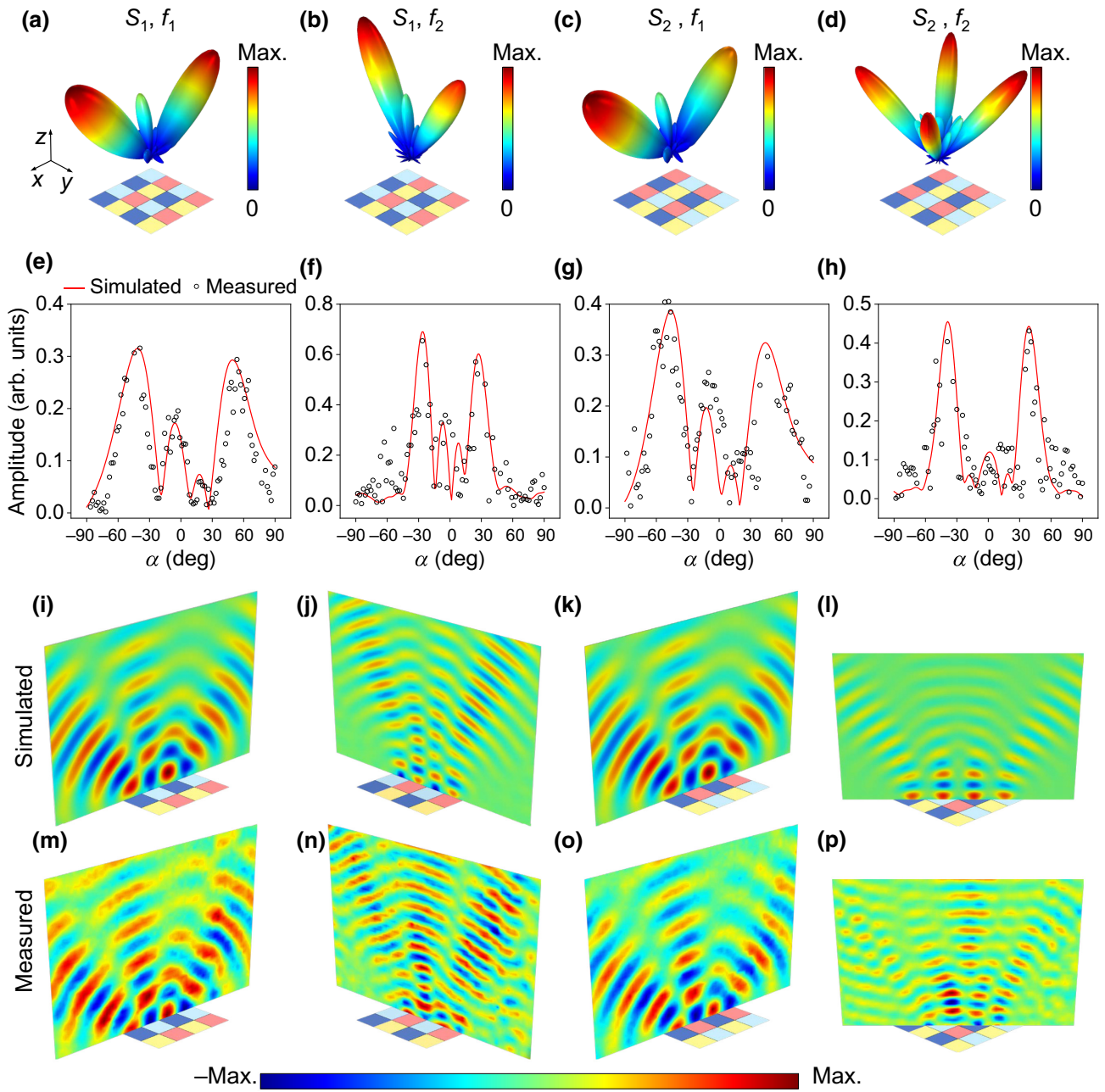


FIG. 3. (a)–(d) Simulated 3D reflected far-field patterns of (a),(b) S_1 and (c),(d) S_2 for (a),(c) f_1 and (b),(d) f_2 . (e)–(h) Simulated (line) and measured (dot) 1D far-field patterns corresponding to (a)–(d), respectively. Simulated (i)–(l) and measured (m)–(p) pressure distributions corresponding to (a)–(d), respectively.

4(f), respectively, with the solid line representing the simulated results and the dashed line representing the measured results. We can see that the energy peak presents a dramatic decline and the relative energy of the peak decreases for f_1 ; while for f_2 , the energy peak disappears and the energy has a uniform distribution in all reflected directions. To compare the efficiencies of diffusion at the two frequencies, we calculate the normalized diffusion coefficients as 0.38 and 0.72 for f_1 and f_2 , respectively, which means that the diffusing efficiency for f_1 is lower than that for f_2 [36].

The frequency-selected acoustic wave diffuser is of great significance in conditions where the high-frequency composition is expected to disperse while the low-frequency composition remains.

C. Frequency-selected generation of airy acoustic beams

Finally, we demonstrate a metasurface that can generate frequency-selected acoustic Airy beams programmed by dual-band coding units. An Airy beam is a type of

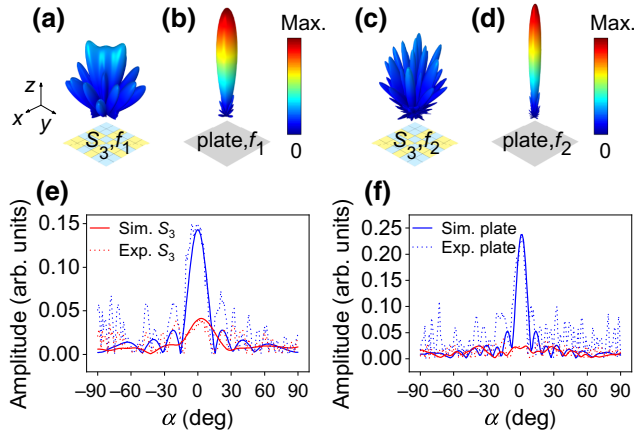


FIG. 4. The simulated 3D reflected far-field patterns of the diffusion coding metasurface S_3 and the plate for (a),(b) f_1 and (c),(d) f_2 . The simulated and measured 1D reflected far-field distributions versus the reflection angle on the x - z plane for (e) f_1 and (f) f_2 .

“nondiffraction” wave packet described by the Airy function [37]. In addition to the nondiffraction and self-healing properties, the Airy beam has a marvelous feature of “self-accelerating” without any external potential, which has been widely applied to wave manipulations in optics and acoustics [37,38]. For a 1D Airy beam, the phase and displacement are expressed as [37,38]

$$\phi = \text{Ai}(bx) \exp(ax + ibx \sin \theta), \quad (4)$$

where $\text{Ai}(bx)$ is the 1D Airy function, k denotes the wave number, a is a positive value to ensure the finite Airy tail when $x \rightarrow \infty$, b is the transverse scale, and θ represents the bending direction. Here, we take

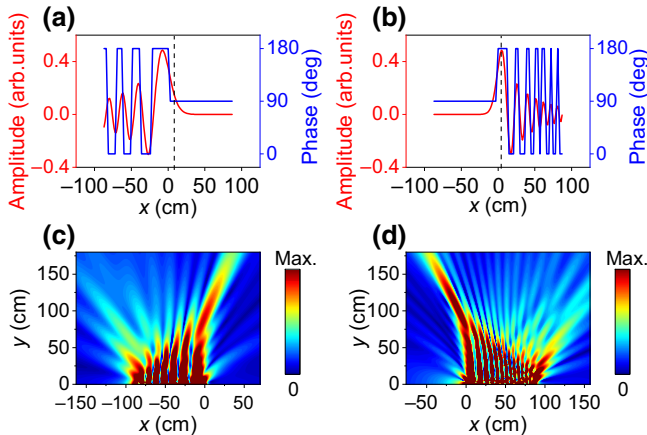


FIG. 5. The Airy functions (red line) and approximate phase distribution (blue line) of the Airy functions with (a) ϕ_1 for f_1 and (b) ϕ_2 for f_2 . (c),(d) The theoretical field distributions of Airy beams generated by approximate phase distributions, shown as blue lines in (a) and (b) for f_1 and f_2 , respectively.

θ equal to 0° , which means that the bending direction of the Airy beam is perpendicular to the metasurfaces; then $\phi_1 = \text{Ai}[(250/21)x] \exp[(25/21)x]$ and $\phi_2 = \text{Ai}[-(500/27)x] \exp[-(50/27)x]$ are used for f_1 and f_2 , respectively, as the red lines shown in Figs. 5(a) and 5(b). To generate the Airy beam with a metasurface, the desired phase distribution can be obtained as $\arg[\phi(x, 0)] = 0^\circ$ for $\phi(x, \theta) \geq 0$, $\arg[\phi(x, 0)] = 180^\circ$ for $\phi(x, \theta) < 0$, which are illustrated as blue lines in Figs. 5(a) and 5(b), respectively. The calculated field distributions of the generated Airy beams are shown in Fig. 5(c) for f_1 and Fig. 5(d) for f_2 . Then, we can discretize the phase distributions to two sequences at the two frequencies and integrate them onto one metasurface utilizing the proposed dual-band coding units. Figure 6(a) exhibits the discrete phase distributions to generate the frequency-selective Airy beams, from which the metasurface with sequence S_4 is acquired.

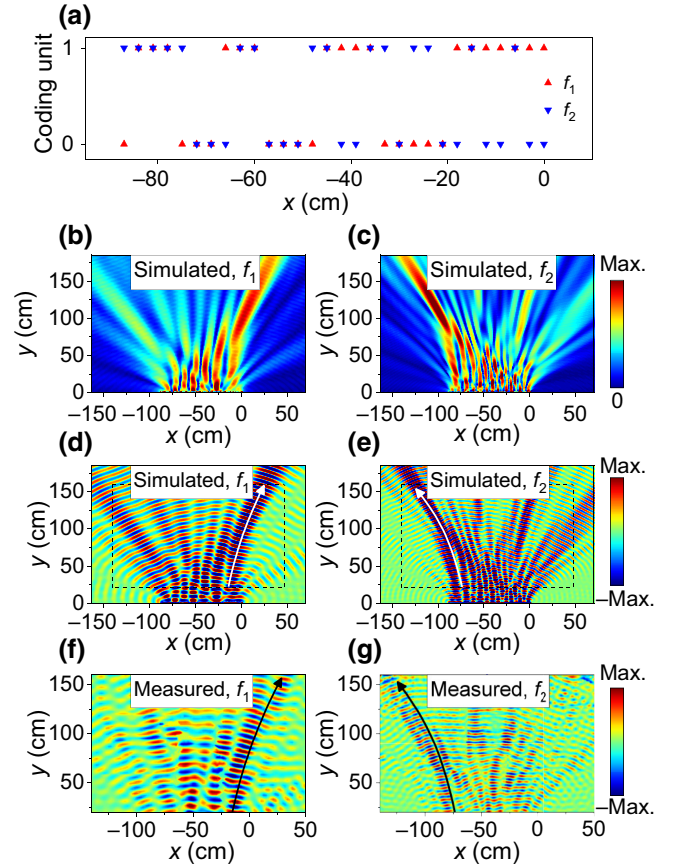


FIG. 6. (a) The discrete phase profile of the designed metasurfaces S_4 to generate the frequency-selective dual-band Airy beams. (b),(c) Simulated field distributions of the reflected Airy beams for f_1 and f_2 , respectively. The corresponding simulated (d),(e) and measured (f),(g) pressure distributions of the reflected Airy beams for f_1 and f_2 , respectively. The areas indicated by the black dashed rectangle are the measurement areas. The white and black arrows in (d)–(g) indicate the bending path of the Airy beams.

The simulated field distributions of S_4 with discrete phases are shown in Figs. 6(b) and 6(c), which are consistent with the simulated results of the continuous phases, indicating that our discretization process is available. The corresponding simulated and measured pressure distributions at f_1 (f_2) are shown in Figs. 6(d) and 6(e) [Figs. 6(f) and 6(g)], respectively, in which an Airy beam bending to the right (left) is observed, with the arrows indicating the bending path. Thus, if the metasurface is normally illuminated by an acoustic wave containing f_1 and f_2 , two Airy beams with opposite bending directions can be obtained, which can be employed to produce nondiffraction frequency-selected acoustic focusing devices.

IV. CONCLUSION

In conclusion, we propose frequency-selected bifunctional-coding metasurfaces based on two-layer Helmholtz-like coding units. The proposed designs are demonstrated to work independently at two frequencies and have two functions at two specific frequencies. To evaluate the frequency-selected bifunctions, frequency-selected anomalous reflection, diffusion, and Airy-beam generation are realized. The proposed frequency-selected bifunctional coding acoustic metasurfaces open up an avenue for frequency-selected multifunctional acoustic devices and have applications in acoustic preservation, imaging, and acoustic wavelength multiplexing devices. Moreover, owing to the resonant mechanism of the proposed dual-band bifunctional coding metasurfaces, the principle can be further extended to the higher frequencies or the elastic waves. Certainly, as the resonant mechanism of the elastic waves in the solid is different from that of the acoustic waves in the resonators immersed in air, the coding unit needs to be redesigned rather than the simple Helmholtz resonators.

ACKNOWLEDGMENTS

This work was supported by the National Key Research and Development Program of China (Grants No. 2016YFA0301102 and No. 2017YFA0303800), the National Natural Science Fund for Distinguished Young Scholar (Grant No. 11925403), the National Natural Science Foundation of China (Grants No. 11974193, No. 91856101, and No. 11774186), the Natural Science Foundation of Tianjin for Distinguished Young Scientists (Grant No. 18JCJJC45700), and the Tianjin Postgraduate Research and Innovation Project (Grant No. 2019YJSB035).

[1] N. Yu, P. Genevet, M. A. Kats, F. Aieta, J. P. Tetienne, F. Capasso, and Z. Gaburro, Light propagation with phase discontinuities: Generalized laws of reflection and refraction, *Science* **334**, 333 (2011).

- [2] L. Huang, X. Chen, H. Mühlenbernd, G. Li, B. Bai, Q. Tan, G. Jin, T. Zentgraf, and S. Zhang, Dispersionless phase discontinuities for controlling light propagation, *Nano Lett.* **12**, 5750 (2012).
- [3] X. Ni, N. K. Emani, A. V. Kildishev, A. Boltasseva, and V. M. Shalaev, Broadband light bending with plasmonic nanoantennas, *Science* **335**, 427 (2012).
- [4] S. Sun, K. Y. Yang, C. M. Wang, T. K. Juan, W. T. Chen, C. Y. Liao, Q. He, S. Xiao, W. T. Kung, G. Y. Guo, L. Zhou, and D. P. Tsai, High-efficiency broadband anomalous reflection by gradient meta-surfaces, *Nano Lett.* **12**, 6223 (2012).
- [5] Z. Li, E. Palacios, S. Butun, and K. Aydin, Visible-frequency metasurfaces for broadband anomalous reflection and high-efficiency spectrum splitting, *Nano Lett.* **15**, 1615 (2015).
- [6] Y. Li, B. Liang, Z. M. Gu, X. Zou, and J. Cheng, Reflected wavefront manipulation based on ultrathin planar acoustic metasurfaces, *Sci. Rep.* **3**, 2546 (2013).
- [7] Y. F. Zhu, X. Y. Zou, R. Q. Li, X. Jiang, J. Tu, B. Liang, and J. Cheng, Dispersionless manipulation of reflected acoustic wavefront by subwavelength corrugated surface, *Sci. Rep.* **5**, 10966 (2015).
- [8] Y. Zhu, J. Hu, X. Fan, J. Yang, B. Liang, X. Zhu, and J. Cheng, Fine manipulation of sound via lossy metamaterials with independent and arbitrary reflection amplitude and phase, *Nat. Commun.* **9**, 1623 (2018).
- [9] K. Tang, C. Qiu, M. Ke, J. Lu, Y. Ye, and Z. Liu, Anomalous refraction of airborne sound through ultrathin metasurfaces, *Sci. Rep.* **4**, 6517 (2014).
- [10] Y. Xie, W. Wang, H. Chen, A. Konneker, B. I. Popa, and S. A. Cummer, Wavefront modulation and subwavelength diffractive acoustics with an acoustic metasurfaces, *Nat. Commun.* **5**, 5553 (2014).
- [11] X. Zhu, K. Li, P. Zhang, J. Zhu, J. Zhang, C. Tian, and S. Liu, Implementation of dispersion-free slow acoustic wave propagation and phase engineering with helical-structured metamaterials, *Nat. Commun.* **7**, 11731 (2016).
- [12] J. Li, P. Yu, C. Tang, H. Cheng, J. Li, S. Chen, and J. Tian, Bidirectional perfect absorber using free substrate plasmonic metasurfaces, *Adv. Opt. Mater.* **5**, 1700152 (2017).
- [13] S. Chen, H. Cheng, H. Yang, J. Li, X. Duan, C. Gu, and J. Tian, Polarization insensitive and omnidirectional broadband near perfect planar metamaterial absorber in the near infrared regime, *Appl. Phys. Lett.* **99**, 253104 (2011).
- [14] Y. Yao, R. Shankar, M. A. Kats, Y. Song, J. Kong, M. Loncar, and F. Capasso, Electrically tunable metasurface perfect absorbers for ultrathin mid-infrared optical modulators, *Nano Lett.* **14**, 6526 (2014).
- [15] Y. Zhu, X. Zou, B. Liang, and J. Cheng, Acoustic one-way open tunnel by using metasurfaces, *Appl. Phys. Lett.* **107**, 113501 (2015).
- [16] C. Shen, Y. Xie, J. Li, S. A. Cummer, and Y. Jing, Asymmetric acoustic transmission through near-zero-index and gradient-index metasurfaces, *Appl. Phys. Lett.* **108**, 223502 (2016).
- [17] Y. Li, C. Shen, Y. Xie, J. Li, W. Wang, S. A. Cummer, and Y. Jing, Tunable Asymmetric Transmission via Lossy Acoustic Metasurfaces, *Phys. Rev. Lett.* **119**, 035501 (2017).

- [18] S. Chen, W. Liu, Z. Li, H. Cheng, and J. Tian, Metasurface-empowered optical multiplexing and multifunction, *Adv. Mater.* **32**, 1805912 (2019).
- [19] X. Chen, P. Liu, Z. Hou, and Y. Pei, Implementation of acoustic demultiplexing with membrane-type metasurface in low frequency range, *Appl. Phys. Lett.* **110**, 161909 (2017).
- [20] Y. Zhu, and B. Assouar, Multifunctional acoustic metasurface based on an array of Helmholtz resonators, *Phys. Rev. B* **99**, 174109 (2019).
- [21] Y. Zhu, X. Fan, B. Liang, J. Yang, J. Yang, L. Yin, and J. Cheng, Multi-frequency acoustic metasurface for extraordinary reflection and sound focusing, *AIP Adv.* **6**, 121702 (2016).
- [22] T. J. Cui, M. Q. Qi, X. Wan, J. Zhao, and Q. Cheng, Coding metamaterials, digital metamaterials and programmable metamaterials, *Light Sci. Appl.* **3**, e218 (2014).
- [23] L. H. Gao, Q. Cheng, J. Yang, S. J. Ma, J. Zhao, S. Liu, H. B. Chen, Q. He, W. X. Jiang, H. F. Ma, Q. Y. Wen, L. J. Liang, B. B. Jin, W. W. Liu, L. Zhou, J. Q. Yao, P. H. Wu, and T. J. Cui, Broadband diffusion of terahertz waves by multi-bit coding metasurfaces, *Light Sci. Appl.* **4**, e324 (2015).
- [24] L. Zhang, R. Y. Wu, G. D. Bai, H. T. Wu, Q. Ma, X. Q. Chen, and T. J. Cui, Transmission-reflection-integrated multifunctional coding metasurface for full-space controls of electromagnetic waves, *Adv. Funct. Mater.* **65**, 3374 (2018).
- [25] S. Liu, L. Zhang, Q. L. Yang, Q. Xu, Y. Yang, A. Noor, Q. Zhang, S. Iqbal, X. Wan, Z. Tian, W. X. Tang, Q. Cheng, J. G. Han, W. L. Zhang, and T. J. Cui, Frequency-dependent dual-functional coding metasurfaces at terahertz frequencies, *Adv. Opt. Mater.* **4**, 1965 (2016).
- [26] L. Zhang, X. Q. Chen, S. Liu, Q. Zhang, J. Zhao, J. Y. Dai, G. D. Bai, X. Wan, Q. Cheng, G. Castaldi, V. Galdi, and T. J. Cui, Space-time-coding digital metasurfaces, *Nat. Commun.* **9**, 4334 (2018).
- [27] L. Zhang, S. Liu, L. Li, and T. J. Cui, Spin-controlled multiple pencil beams and vortex beams with different polarizations generated by Pancharatnam-Berry coding metasurfaces, *ACS Appl. Mater. Interfaces* **9**, 336447 (2017).
- [28] L. Li, T. J. Cui, W. Ji, S. Liu, J. Ding, X. Wan, Y. B. Li, M. Jiang, C. W. Qiu, and S. Zhang, Electromagnetic reprogrammable coding metasurface holograms, *Nat. Commun.* **8**, 197 (2017).
- [29] B. Xie, K. Tang, H. Cheng, Z. Liu, S. Chen, and J. Tian, Coding acoustic metasurfaces, *Adv. Mater.* **29**, 1603507 (2017).
- [30] B. Xie, H. Cheng, K. Tang, Z. Liu, S. Chen, and J. Tian, Multiband asymmetric transmission of airborne sound by coded metasurfaces, *Phys. Rev. Appl.* **7**, 024010 (2017).
- [31] Y. Zhang, B. Xie, W. Liu, H. Cheng, S. Chen, and J. Tian, Anomalous reflection and vortex beam generation by multi-bit coding acoustic metasurfaces, *Appl. Phys. Lett.* **114**, 091905 (2019).
- [32] M. Ma, Z. Li, W. Liu, C. Tang, Z. Li, H. Cheng, J. Li, S. Chen, and J. Tian, Optical information multiplexing with nonlinear coding metasurfaces, *Laser Photonics Rev.* **13**, 1900045 (2019).
- [33] J. P. Xia, D. Jia, H. X. Sun, S. Q. Yuan, Y. Ge, Q. R. Si, and X. J. Liu, Programmable coding acoustic topological insulator, *Adv. Mater.* **30**, 1805002 (2018).
- [34] COMSOL MULTIPHYSICS, Version 5.4, COMSOL, Inc., Burlington, MA, 2018.
- [35] M. Schroeder, Binaural dissimilarity and optimum ceilings for concert halls: More lateral sound diffusion, *J. Acoust. Soc. Am.* **65**, 958 (1979).
- [36] Y. Zhu, X. Fan, B. Liang, J. Cheng, and Y. Jing, Ultrathin Acoustic Metasurface-Based Schroeder Diffuser, *Phys. Rev. X* **7**, 021034 (2017).
- [37] Z. Li, H. Cheng, Z. Liu, S. Chen, and J. Tian, Plasmonic Airy beam generation by both phase and amplitude modulation with metasurfaces, *Adv. Opt. Mater.* **4**, 1230 (2016).
- [38] H. Gao, Z. Gu, B. Liang, X. Zou, J. Yang, J. Yang, and J. Cheng, Acoustic focusing by symmetrical self-bending beams with phase modulations, *Appl. Phys. Lett.* **108**, 073501 (2016).